Available online at www.sciencedirect.com
ScienceDirect
Journal of Computational Physics 227 (2008) 4977–4997
JOURNAL OF COMPUTATIONAL PHYSICS
www.elsevier.com/locate/jcp

Three-dimensional Eulerian method for large deformation of viscoelastic fluid: Toward plate-mantle simulation

Mikito Furuichi *, Masanori Kameyama, Akira Kageyama

Earth Simulator Center, Japan Agency for Marine-Earth Science and Technology (JAMSTEC), 3173-25 Showa-machi, Kanazawa-ku, Yokohama 236-0001, Japan

Received 7 May 2007; received in revised form 13 December 2007; accepted 20 January 2008
Available online 9 February 2008

Abstract

Toward the unified simulation of the large deformation of a rigid viscoelastic material (plate) and the convection of a viscous fluid (mantle), an Eulerian scheme with a semi-Lagrangian method is developed. The scheme adopts the CIP-CSLR method for advection terms of staggered grid system in three dimensions. The positive transported profile of a positive quantity is assured by flux corrections in the dimensional splitting method. The Jaumann co-rotational effect of the stress tensor is also integrated into the semi-Lagrangian treatment. This co-rotated semi-Lagrangian method is combined with an exponential time differencing method in the time development of the Maxwell constitutive model. The large time step comparable to, or larger than, the Maxwell relaxation time is successfully realized. Validation tests are performed for the three-dimensional Rayleigh–Taylor instability of a viscoelastic material with jump discontinuity of the mass density and other material properties.

Keywords: CIP; Directional splitting method; Flux correction; Viscoelasticity; Mantle convection; Exponential time differencing

1. Introduction

One of the most important problems in geodynamics is how and why the plate tectonics occurs on the Earth. The basic concept in the theory of plate tectonics is that the outer shell of the Earth is divided into a number of thin rigid plates which are in relative motion with respect to one another (e.g. [1,2]). Plate tectonics provides a general framework for understanding geophysical and/or geological phenomena observed at the Earth's surface, such as worldwide distribution of seismicity, volcanism and mountain building (e.g. [3]). As revealed by space missions, plate tectonics is unique to the Earth: There is no direct evidence of the features relevant to plate tectonics, such as extensive ridges or trench systems, on other terrestrial planets (e.g. [4]). The fact that the plates are formed at mid-ocean ridges, move away from the ridges, and recirculate into the mantle through trenches implies that the motion of surface plates is a part of the convection in the underlying mantle.

* Corresponding author.
E-mail address: m-furuic@jamstec.go.jp (M. Furuichi).

0021-9991/$ - see front matter © 2008 Elsevier Inc. All rights reserved.
doi:10.1016/j.jcp.2008.01.052

Since a numerical modeling of mantle convection first arose [5,6], much effort has been devoted so far to the reproduction of plate tectonics in the numerical models of mantle convection (see [7,8] for reviews).

Unfortunately, however, ordinary fluid-dynamical approaches to mantle convection simulations have not been very successful in the reproduction of plate tectonics. The major difficulty comes from the difference in the rheological characters between the plates and mantle. The motions in the mantle are well described by the flow of viscous fluid whose viscosity is typically 10^{19}–10^{21} Pa s [2,9]. On the other hand, the rheology needed to describe a large deformation in the tectonic plates is highly non-linear. In particular, an elasticity is expected to affect the deformation processes near the surface, where temperature is sufficiently low. It is therefore important to develop numerical techniques that can deal with a flow and/or a large deformation of fluids with elastic property, in order to step forward toward the plate-mantle simulation.

The key issue to the treatment of viscoelastic plate-like materials is a choice of numerical schemes for advection equations. In order to advect physical quantities which may have sharp contrasts (such as stress and viscosity), it is required to employ advection schemes with low numerical diffusion. Since low diffusive Eulerian schemes generally employ high-order interpolated functions and have an unwanted oscillatory behavior of a profile according to Godunov's order barrier theorem [10,11], Eulerian approaches have not been widely used in the numerical models of viscoelasticity [12]. Instead, some models use a Lagrangian frame of reference, where the computational meshes are defined on the boundary of a physical contrast and move with the material point [13–15]. In these models, a large deformation is handled by remeshing procedures. On the other hand, particle-based semi-Lagrangian methods are employed by many applications [16–19], where advection equations are solved in a Lagrangian manner by tracer particles which construct subgrid scale profiles, while other equations (e.g., the equation of motion) are solved on the Eulerian mesh via remapping procedures. Hybrid method of particle-based remeshing procedures in a Lagrangian method is also proposed [20].

In this paper we present a numerical algorithm for large deformation of viscoelastic fluid motions in a Eulerian frame of reference. Our method is based on the Conservative semi-Lagrangian advection scheme of Constrained Interpolation Profile (CIP) method with Rational function (CIP-CSLR), proposed by Yabe and coworkers [21–29]. The CIP-CSLR is widely used in many fields to numerically solve advection problems keeping the sharpness of the profile of the transported quantity without the oscillatory behavior. We have discussed how to use the CIP-CSLR method in staggered grid systems in three dimensions. A flux correction is newly proposed to guarantee the non-negative distribution of a non-negative scalar, such as the mass density. Compared with other flux correction schemes reported so far (e.g. [30,31]), our scheme is simple and, at the same time, easy to implement. On the other hand, in order to enhance the applicability of the CIP-CSLR to viscoelastic problems, we have improved a semi-Lagrangian treatment of the Jaumann co-rotational derivative of the stress tensor. The Jaumann co-rotational derivative is taken into account to satisfy the material objectivity of the stress tensor in a finite deformation of a viscoelastic material.

In the next section, we explain a physical model for a Maxwell viscoelastic material. In Section 3, we introduce the solution algorithms of semi-Lagrangian scheme for scalar and tensor variables, and the treatment of the viscoelastic constitutive equation. Then in Section 4, we discuss results of several cases of the three-dimensional Rayleigh–Taylor instability test. We summarize the results in Section 5.

2. Physical model

We consider a motion of incompressible fluid with Maxwell viscoelasticity in three-dimensional Cartesian geometry $(x_1 = x, x_2 = y, x_3 = z)$. Since a slowly creeping motion is assumed, both the non-linear and time-derivative terms of velocity are ignored in the equation of motion. We solve the Stokes equation

$$-\frac{\partial p}{\partial x_i} + \frac{\partial \tau_{ij}}{\partial x_j} + f_i = 0, \quad (i, j = 1, 2, 3) \tag{1}$$

under the incompressible condition

$$\frac{\partial v_i}{\partial x_i} = 0, \tag{2}$$

where p is the pressure, v_i and f_i are the velocity and body force in ith direction, respectively. The deviatoric stress tensor τ_{ij} is given by the viscoelastic Maxwell constitutive equation

$$\tau_{ij} + \lambda \overset{\circ}{\tau}_{ij} = 2\eta d_{ij}, \tag{3}$$

where η is the shear viscosity, λ is the Maxwell relaxation time and d_{ij} is the stretching tensor defined by

$$d_{ij} = \frac{1}{2}\left(\frac{\partial v_i}{\partial x_j} + \frac{\partial v_j}{\partial x_i}\right). \tag{4}$$

The term $\overset{\circ}{\tau}_{ij}$ denotes the Jaumann co-rotational rate of the stress tensor, which is written by

$$\overset{\circ}{\tau}_{ij} = \frac{\partial \tau_{ij}}{\partial t} + v_k \frac{\partial \tau_{ij}}{\partial x_k} - w_{ik}\tau_{kj} + \tau_{ik} w_{kj}, \tag{5}$$

with the spin tensor

$$w_{ij} = \frac{1}{2}\left(\frac{\partial v_i}{\partial x_j} - \frac{\partial v_j}{\partial x_i}\right). \tag{6}$$

The Jaumann rate is introduced to satisfy the principle of material objectivity during the deformation processes. A transport of the fluid material is described by the conservative equation

$$\frac{\partial \Gamma}{\partial t} = -\frac{\partial (v_i \Gamma)}{\partial x_i} = -v_i \frac{\partial \Gamma}{\partial x_i}, \tag{7}$$

where Γ is a property, for example density or viscosity, of the fluid.

3. Numerical scheme

3.1. semi-Lagrangian scheme for transport of variables

When one considers large deformation of a viscoelastic material that exhibits a sharp interface of rheological properties, the numerical accuracy of advection terms is critically important. Since we construct an advection scheme for viscoelastic fluid by CIP-CSLR method proposed by Yabe et al. [25,26], we briefly introduce the basic CIP-CSLR method [21–24], followed by the description of our treatment in three-dimensional staggered grid coordinate.

3.1.1. CIP-CSLR method

A one-dimensional semi-Lagrangian scheme solves an advection equation of a variable f

$$\frac{\partial f}{\partial t} = -v \frac{\partial f}{\partial x}, \tag{8}$$

separately from other (non-advective) terms. The CIP-CSL method solves Eq. (8) with conserving a spatial integration value $\int f \, dx$ in a flux form. There are two variants of the CIP-CSL method, called CIP-CSL4 and CIP-CSL2. We focus on the CIP-CSL2 (hereafter denoted simply by CIP-CSL) in this paper. The definition of variables in one dimension is shown in Fig. 1, where f_i and $\rho_{i+\frac{1}{2}}$ are a point value and cell integrated value, respectively. In the CIP-CSL method, we take into account the integrals $D_i(x)(x_{i-1} \leqslant x \leqslant x_{i+1})$ and $\rho_{i+\frac{1}{2}}$ as follows,

$$D_i(x) = \int_{x_i}^{x} f(x)\,dx \cong \int_{x_i}^{x} F_{icell}(x)\,dx, \quad \rho_{i+\frac{1}{2}} = \int_{x_i}^{x_{i+1}} F_{i+\frac{1}{2}}(x)\,dx, \tag{9}$$

where $icell = i + \mathrm{sgn}(x - x_i)/2$, and the real profile $f(x)$ between the grid points is approximated by a piecewise profile $F_{icell}(x)(x_{icell-\frac{1}{2}} \leqslant x \leqslant x_{icell+\frac{1}{2}})$. In contrast that $F_{icell}(x)$ is interpolated by a cubic polynomial (or a rational function) in the original CIP (or RCIP) method [21,24], the cubic interpolation is applied to its integral $D_i(x)$ in the CIP-CSL method. Denoting $D_i(x)$ at nth time step by $D_i^n(x)$, it satisfies the following four conditions;

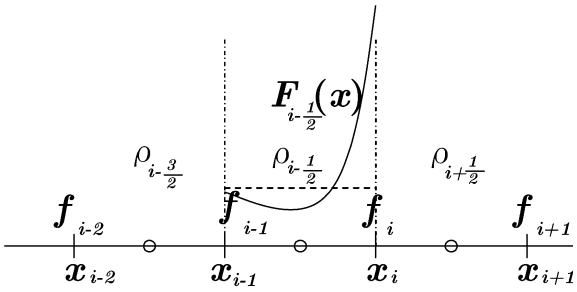

Fig. 1. Definition of variables in one-dimensional advection.

$$D_i^n(x_i) = 0, \quad D_i^n(x_{iup}) = isg\rho_{icell}^n,$$
$$\left.\frac{\partial D_i^n(x)}{\partial x}\right|_{x=x_i} = F_{icell}^n(x_i) = f_i^n, \qquad \left.\frac{\partial D_i^n(x)}{\partial x}\right|_{x=x_{iup}} = F_{icell}^n(x_{iup}) = f_{iup}^n, \tag{10}$$

where $isg = \mathrm{sgn}(x - x_i), iup = i + isg$. The time evolution of $\rho_{i+\frac{1}{2}}^n$ is given by

$$\rho_{i+\frac{1}{2}}^{n+1} = \rho_{i+\frac{1}{2}}^n + D_{i+1}^n(x_{i+1} - v_{i+1}\Delta t) - D_i^n(x_i - v_i\Delta t), \tag{11}$$

which comes from the conservation of the total mass over the grid cell. The non-advective equations of Eqs. (1) and (3) at nth time step are solved with the cell integrated value $\rho_{i+\frac{1}{2}}^n$ of fluid property. On the other hand, the point value f_i^{n+1} is updated in ordinary semi-Lagrangian manner

$$f_i^{n+1} = f_i^* \equiv \frac{\partial D_i^n(x_i - v_i\Delta t)}{\partial x}, \tag{12}$$

in the mass transport of incompressible fluid.

The CIP-CSLR method is a variant of CIP-CSL method. Two types of the CIP-CSLR method are proposed in Ref. [28], and here we employ the CSLR1 [26,28]. The CIP-CSLR adopts a modified rational functions for the interpolation,

$$D_i^n(x) = \frac{a_i(x - x_i) + b_i(x - x_i)^2 + c_i(x - x_i)^3}{1 + \beta_i(x - x_i)}, \tag{13}$$

so as to reduce a numerical oscillation of a profile. The coefficients of Eq. (13) are decided by (10) as follows:

$$a_i = f_i^n, \tag{14}$$
$$b_i = \frac{(1 + \beta_i\Delta x_i)(2S_{icell} - f_{iup}^n) + S_{icell} - 2f_i^n}{\Delta x}, \tag{15}$$
$$c_i = \frac{(1 + \beta_i\Delta x_i)(f_{iup}^n - S_{icell}) - S_{icell} + f_i^n}{\Delta x^2}, \tag{16}$$
$$\beta_i = \left[\frac{|S_{icell} - f_i^n| + \epsilon}{|f_{iup}^n - S_{icell}| + \epsilon} - 1\right]/\Delta x, \tag{17}$$

where $\Delta x = x_{iup} - x_i, S_{icell} = \rho_{icell}/|\Delta x|$, and a small positive value ϵ is introduced to numerically avoid a divergence of denominator when $(f_{iup}^n - S_{icell}) = 0$ [28,29].

If $(f_{iup}^n - S_{icell})(S_{icell} - f_i^n) \geqslant 0, D_i^n(x)$ is expressed by the rational function with the coefficient $c_i = 0$, and proved to preserve the monotones of profile in Ref. [24]. On the other hand, when $(f_{iup}^n - S_{icell})(S_{icell} - f_i^n) < 0$, the profile have a peak or valley in the grid cell, and is expressed by the function (13) with the coefficient $c_i \neq 0$ (when $\beta_i = 0$, the function is cubic polynomial). We note that an oscillatory behavior can appear from such a peak or valley in the grid cell, and may break a physical requirement for a transported quantity such as a positiveness of a scalar (e.g., viscosity or mass).

3.1.2. Separation test in one dimension

For the purpose of understanding the oscillatory behavior of the case with $(f^n_{iup} - S_{icell})(S_{icell} - f^n_i) < 0$, for a moment, we forget the incompressibility and consider the simple one-dimensional advection problem. Fig. 2 illustrates the calculation setup in which a profile is divided into two pieces at $i = i_b$ with $|\Delta x| = 1.0$ and $\Delta t = 0.1$. The velocity and initial profile of $(\rho^n_{i+\frac{1}{2}}, f^n_i)$ are given by

$$\begin{aligned} &v_i = -1.0, \quad f^0_i = 1.0, \quad \rho^0_{i+\frac{1}{2}} = 1.0 \quad \text{for } i < i_b, \\ &v_i = 1.0, \quad f^0_i = 1.0, \quad \rho^0_{i+\frac{1}{2}} = 1.0 \quad \text{for } i > i_b, \\ &v_i = 1.0, \quad f^0_i = 1.0, \quad \rho^0_{i+\frac{1}{2}} = \rho_{\text{center}} \quad \text{for } i = i_b. \end{aligned} \tag{18}$$

A valley profile with the depth of ρ_{center} is initially placed at i_bth grid cell. In Table 1, we show the result after one time step advective calculation and the minimum value during 15 time steps calculation. It is found that the interpolated function with $c_i \neq 0$ at $i = i_b$ starts to oscillate as deepen the initially given valley and produces the negative value state in the transport of positive defined value.

Such a problematic valley profile can be created, for example when a low density of the profile is locally introduced by a physical model in non-advection term. Moreover, in the following subsections (Sections 3.1.3 and 3.1.4), we will show that the temporal step of our multi-dimensional advection procedure may produce a deeper valley than that in one-dimensional advection.

3.1.3. Fractional step technique for multi-dimensional staggered grid system

We perform the multi-dimensional calculation by following the study of [26], in which the one-dimensional advective procedure is applied to every direction. For the simplicity, we explain our directional splitting

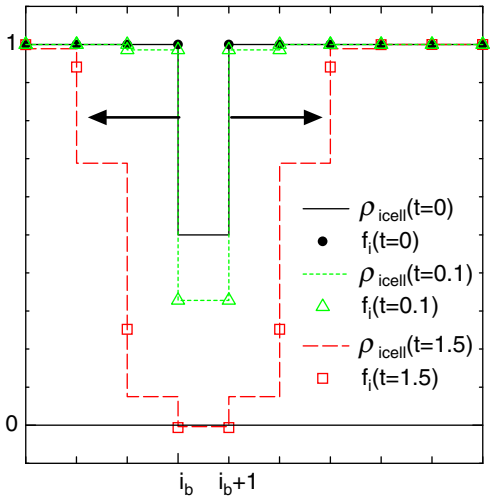

Fig. 2. One-dimensional calculation setup in which profile is divided into two pieces at $i = i_b$.

Table 1
Result of one-dimensional separation test

ρ_{center}	$\rho^1_{i_b+\frac{1}{2}}$	Minimum value of $\rho^{1-15}_{i_b+\frac{1}{2}}$
1.0	0.80	$\rho^{14}_{i_b+\frac{1}{2}} = -5.82\text{E}-3$
0.5	0.33	$\rho^{9}_{i_b+\frac{1}{2}} = -1.25\text{E}-2$
0.25	9.20E−2	$\rho^{5}_{i_b+\frac{1}{2}} = -6.72\text{E}-2$
0.125	−2.60E−2	$\rho^{4}_{i_b+\frac{1}{2}} = -0.128$
0.0	−0.144	$\rho^{3}_{i_b+\frac{1}{2}} = -0.210$

The cell integrated value of nth time step at bottom of the valley are given by $\rho^n_{i_b+\frac{1}{2}}$. Setup is shown in Fig. 2.

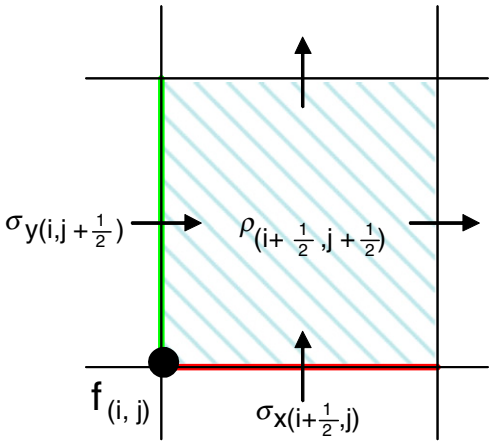

Fig. 3. Cartesian staggered grid in two dimensions.

procedure in two dimensions. The Cartesian staggered grid is employed (Fig. 3), in which $f_{(i,j)}$, $\sigma_{x(i+\frac{1}{2},j)}$, $\sigma_{y(i,j+\frac{1}{2})}$ and $\rho_{(i+\frac{1}{2},j+\frac{1}{2})}$ are defined as the point value, line integrated value and cell integrated value, respectively.

The procedure of two-dimensional advection is as follows:

– x direction
  1st: advect the (f^n, σ_x^n) to (f^*, σ_x^*) with the velocity $v^*_{x(i,j)} = (v_{x(i,j+\frac{1}{2})} + v_{x(i,j-\frac{1}{2})})/2$.
  2nd: advect the (σ_y^n, ρ^n) to (σ_y^*, ρ^*) with the velocity $v^{**}_{x(i,j+\frac{1}{2})}$.

– y direction
  3rd: advect the (f^*, σ_y^*) to $(f^{n+1}, \sigma_y^{n+1})$ with the velocity $v^*_{y(i,j)} = (v_{y(i+\frac{1}{2},j)} + v_{y(i-\frac{1}{2},j)})/2$.
  4th: advect the (σ_x^*, ρ^*) to $(\sigma_x^{n+1}, \rho^{n+1})$ with the velocity $v^{**}_{y(i+\frac{1}{2},j)}$.

Analogously, the three-dimensional advection is implemented in the staggered grid system.

If we follow the original fractional step method of Ref. [26], the averaged velocities at cell interfaces

$$\begin{aligned} v^{**}_{x(i,j+\frac{1}{2})} &= v^{\text{ave}}_{x(i,j+\frac{1}{2})} = (v^*_{x(i,j)} + v^*_{x(i,j+1)})/2, \\ v^{**}_{y(i+\frac{1}{2},j)} &= v^{\text{ave}}_{y(i+\frac{1}{2},j)} = (v^*_{y(i,j)} + v^*_{y(i+1,j)})/2, \end{aligned} \tag{19}$$

are used in 2nd and 4th advection steps. However it is found that the averaged velocity diffuses the shear of the original velocity $(v_{x(i,j+\frac{1}{2})}, v_{y(i+\frac{1}{2},j)})$ defined on the staggered grid. Instead of (19), we employ the same velocity (raw velocity) at cell interfaces as

$$v^{**}_{x(i,j+\frac{1}{2})} = v_{x(i,j+\frac{1}{2})}, \quad v^{**}_{y(i+\frac{1}{2},j)} = v_{y(i+\frac{1}{2},j)}. \tag{20}$$

3.1.4. Separation test in two dimensions

For a comparison of two types of velocity of (19) and (20) in detail, we conduct a simple experiment of two dimensional separation, illustrated in Fig. 4. A set of smooth profile

$$f_{(i,j)} = 1.0, \quad \sigma_{x(i+\frac{1}{2},j)} = \sigma_{y(i,j+\frac{1}{2})} = 1.0, \quad \rho_{(i+\frac{1}{2},j+\frac{1}{2})} = 1.0, \tag{21}$$

is employed as an initial condition with $|\Delta x| = 1.0$, and a velocity on the staggered grid is given by

$$\begin{aligned} (v_{x(i,j+\frac{1}{2})}, v_{y(i+\frac{1}{2},j)}) &= (-1.0, 1.0) \quad \text{for } (j > i), \\ (v_{x(i,j+\frac{1}{2})}, v_{y(i+\frac{1}{2},j)}) &= (-1.0, -1.0) \quad \text{for } (i = j), \\ (v_{x(i,j+\frac{1}{2})}, v_{y(i+\frac{1}{2},j)}) &= (1.0, -1.0) \quad \text{for } (j < i), \end{aligned} \tag{22}$$

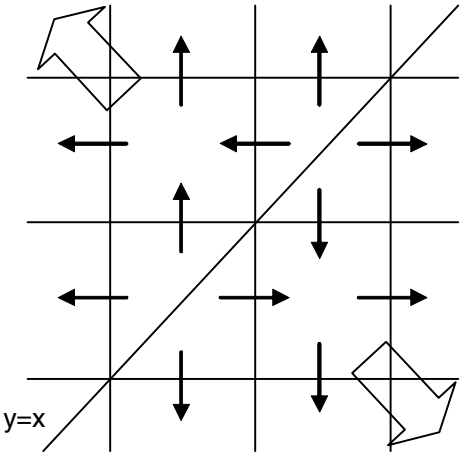

Fig. 4. Two-dimensional calculation setup in which profile is divided into two pieces along $x = y$.

which tears the profile into two pieces along $x = y$, and the calculation is done with a time step $\Delta t = 0.05$. This separation with the divergent of velocity in two dimensions is possible situation for a temporal step of three-dimensional advection of incompressible fluid.

In the 1st step of directional splitting method, the velocities around the cell of the separation ($i = j$) are

$$v^*_{x(i,i)} = 0, \quad v^*_{x(i+1,i)} = 1.0, \quad v^*_{x(i,i+1)} = -1.0, \quad v^*_{x(i+1,i+1)} = 0, \tag{23}$$

and the advection in the 2nd step is done by the averaged velocity

$$v^{**}_{x(i,i+\frac{1}{2})} = v^{\mathrm{ave}}_{x(i,i+\frac{1}{2})} = -0.5, \quad v^{**}_{x(i+1,i+\frac{1}{2})} = v^{\mathrm{ave}}_{x(i+1,i+\frac{1}{2})} = 0.5, \tag{24}$$

or raw velocity

$$v^{**}_{x(i,i+\frac{1}{2})} = v_{x(i,i+\frac{1}{2})} = -1.0, \quad v^{**}_{x(i+1,i+\frac{1}{2})} = v_{x(i+1,i+\frac{1}{2})} = 1.0. \tag{25}$$

The velocity in y direction for the 3rd and 4th advection steps are also obtained in the same manner.

Fig. 5 provides the differences in the time development of the cell integrated value $\rho_{i+\frac{1}{2},i+\frac{1}{2}}$ by a choice of the velocity. It is shown that the decrease of the cell value with the averaged velocity (blue triangle) is slower than

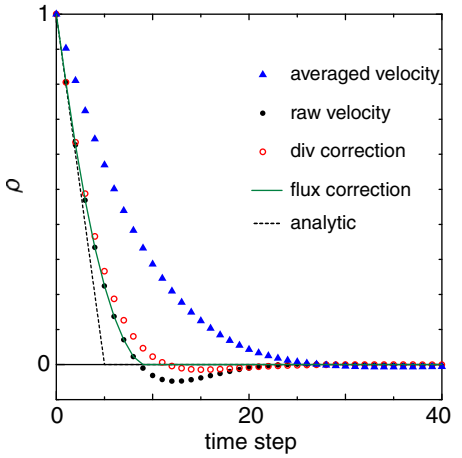

Fig. 5. Time evolutions of the cell integrated value at separation point $\rho^n_{i+\frac{1}{2},i+\frac{1}{2}}$ in advection test of Fig. 4. Result of "analytic" means that cell integrated value is reduced by constant flux (i.e. $\rho^{n+1}_{i+\frac{1}{2},i+\frac{1}{2}} - \rho^n_{i+\frac{1}{2},i+\frac{1}{2}} = 0.2$).

that with the raw velocity (black circle), because the averaged velocity at cell interface (i.e. $|v_x^{**}| = |v_x^{\text{ave}}| = 0.5$) is smaller than raw velocity (i.e. $|v_x^{**}| = |v_x| = 1.0$). This indicates that an edge profile is diffused by using the averaged velocity, whereas our advection with raw velocity can captures the clear separation.

In Table 2, we summarize the minimum cell integrated values during the 40 time steps calculation. It is shown that a negative value by the averaged velocity method keeps in the same order as one-dimensional case (Table 1): by contrast the negative profile by raw velocity is in one order bigger than that by averaged velocity or one-dimensional advection. Because of the large velocity at the cell interface at the trench, the raw velocity method forms a deeper valley than that by the averaged velocity and produces larger negative value profiles.

These results indicate that the low diffusiveness of our multi-dimensional treatment with raw velocity not only leads to the advantage in getting the sharp edges of profile, but also have the fear of producing an unwanted negative profile.

The above oscillatory behavior is improved by a non-advective treatment for the temporal velocity divergence, which is introduced, instead of (12), by

$$f_i^{n+1} = f_i^* - f_i^* \left.\frac{\partial v}{\partial x}\right|_{x=x_i} \mathrm{d}t = f_i^* \left[1 - \left(\frac{v_{i+1} - v_{i-1}}{x_{i+1} - x_{i-1}}\right)\mathrm{d}t\right]. \tag{26}$$

The result with the correction of (26) and the raw velocity is also given in Fig. 5 (red opened circle) and Table 2. However even the divergent treatment can not perfectly prevent the negative oscillatory behavior.

3.1.5. Flux correction scheme for non-negative profile

We propose a remedy for the breaking of the positiveness of a transported quantity by the CIP-CSLR. A careful observation of Eq. (11) suggests that an advection phase can yield the (unphysical) negative $\rho^n_{i+\frac{1}{2}}$ either (i) at the downstream cell when the incoming mass flow is negative owing to the oscillation of the profile, or (ii) at the upstream cell when the amount of outgoing flow is too large. In order to avoid these two possibilities and to realize more precise propagation of non-negative values, we propose the following two kinds of flux corrections. The first one is an explicit cut-off correction (hereafter denoted by "negative-cut" correction) given by

$$\begin{cases} D_i^n(x_i - v_i\Delta t) & = isg\ \mathrm{Max}[isgD_i^n(x_i - v_i\Delta t), 0], \\ F_{icell}^n(x_i - v_i\Delta t) & = \mathrm{Max}[F_{icell}^n(x_i - v_i\Delta t), 0]. \end{cases} \tag{27}$$

The second correction is a diffusive-type (hereafter denoted by "diffuse-flow" correction) given by

$$D_i^n(x_i - v_i\Delta t) = isg\ \mathrm{Min}[isgD_i^n(x_i - v_i\Delta t), \alpha_c\rho_{icell}^n], \tag{28}$$

where α_c is a dimensionless constant, or switching parameter. The negative-cut corrections in Eq. (27) simply prohibit the unphysical negative flux and value at the grid point. The diffuse-flow correction in Eq. (28) invokes an artificial diffusion of the numerical overshoot in the cell, thus preventing the flow from depriving too much mass from the grid cell. The switching parameter α_c is chosen to be the maximum value that guarantees the positiveness of the cell integrated value $\rho^{n+1} \geqslant 0$ in (28). In one-dimensional case, $\alpha_c = 0.5$ is a reasonable choice, since the cell integrated value $\rho_{i-\frac{1}{2}}$ in the next step is assured to be non-negative even if the profile in a cell is drawn by a pair of outgoing flows on the both sides of the cell boundary.

Our diffuse-flow correction is applied not only to the profile of $(f_{iup}^n - S_{icell})(S_{icell} - f_i^n) < 0$ which may produce the unwanted oscillatory behavior, but also to the oscillationless profile of $(f_{iup}^n - S_{icell})(S_{icell} - f_i^n) \geqslant 0$.

Table 2
Summary of minimum value in two-dimensional separation test

	Minimum value of $\rho^{1\sim40}_{(i+\frac{1}{2},i+\frac{1}{2})}$
Averaged velocity	$\rho^{35}_{(i+\frac{1}{2},i+\frac{1}{2})} = -7.11\text{E}-3$
Raw velocity	$\rho^{12}_{(i+\frac{1}{2},i+\frac{1}{2})} = -4.75\text{E}-2$
Divergent velocity treatment with raw velocity	$\rho^{15}_{(i+\frac{1}{2},i+\frac{1}{2})} = -1.47\text{E}-2$

Minimum cell integrated value $\rho^n_{(i_b+\frac{1}{2},i_b+\frac{1}{2})}$ presented in Fig. 5.

One may think that our method breaks the low diffusive character of the interpolation by the rational function. However we can retain the low diffusiveness of CIP-CSLR profile, if the CFL number is a sufficiently small ($\leqslant 0.2$, for example, and details are given in Appendix A).

The result of the separation test in Fig. 5 shows that our flux correction scheme (green line) successfully propagate the non-negative profile without losing the good characters of the CIP-CSLR advection. Our corrective scheme is a kind of flux correction method [30,31] arranged for the CIP-CSLR in the application to slowly moving material.

3.2. Co-rotated semi-Lagrangian method for stress tensors

In our scheme, not only the scalar viscosity but also the deviatoric stress tensor, which are defined on the Cartesian staggered grid [32], are transported by the semi-Lagrangian scheme. The Jaumann co-rotational rate of the stress tensor, Eq. (5), is split into two steps in a semi-Lagrangian way; the advectional step

$$\frac{\partial \tau_{ij}^{*}}{\partial t} = -v_k \frac{\partial \tau_{ij}}{\partial x_k}, \tag{29}$$

and the co-rotational step

$$\frac{\partial \tau_{ij}^{**}}{\partial t} = -\omega_{ik}\tau_{kj}^{*} + \tau_{ik}^{*}\omega_{kj}. \tag{30}$$

The advection step of Eq. (29) is integrated by the standard semi-Lagrangian technique.

The numerical error of the co-rotational step of Eq. (30) is not negligible when it is explicitly integrated in time by, for example,

$$\tau_{ij}^{**} = \tau_{ij}^{*} + \Delta t(-w_{ik}\tau_{kj}^{*} + \tau_{ik}^{*}w_{kj}). \tag{31}$$

We have found that the numerical error can be reduced when the co-rotational step of Eq. (30) is integrated after rewriting it into the form of the rotation of the tensor components (see Appendix B):

$$\tau_{ij}^{**} = R_{ni}\tau_{nm}^{*}R_{mj} = \boldsymbol{R}^{\mathrm{T}}\boldsymbol{\tau}^{*}\boldsymbol{R}, \tag{32}$$

where $\boldsymbol{R}$ is the rotational matrix defined by

$$\boldsymbol{R} = \mathrm{e}^{\boldsymbol{w}\Delta t} = \sum_{m=0}^{\infty} \frac{1}{m!}(\boldsymbol{w}\Delta t)^m. \tag{33}$$

In the actual calculations, $\boldsymbol{R}$ is replaced with $\boldsymbol{R}_n$, by truncating the infinite series of the right-hand side of Eq. (33) up to $m = n$.

In order to demonstrate the accuracy of our semi-Lagrangian treatment for the advection and co-rotation, we perform a one-dimensional circular propagation test (Fig. 6) for two-dimensional stress components (τ_{xx}, τ_{xy}) by the Jaumann co-rotational term of Eq. (5) with a constant angular velocity Ω. In this test, an initial square shape profile of τ_{xx} is advected by Eq. (29) along the azimuthal direction θ, and mixed (rotated) with the profile of τ_{xy} by Eq. (30). We employ either the RCIP [23] or first-order upwind method for the advection. The co-rotational effects are evaluated either by Eq. (33) with a third order rotational matrix $\boldsymbol{R}_3$ or by a difference

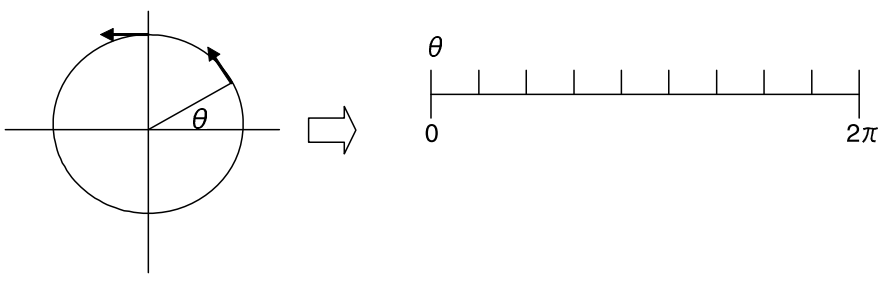

Fig. 6. Schematic picture of one-dimensional propagation test of two-dimensional stress tensor in Fig. 5.

form where the rotational effect is calculated by Eq. (31). We avoid implicit method here, since they lead to practically unfeasible formulations in three-dimensional problems by additional mixed tensor terms. The matrix for the discretized Stokes equation is too complicated to invert.

Fig. 7 shows the mixed states of the propagated tensor components (τ_{xx}, τ_{xy}) on the θ axis. We can see that the transport by the RCIP (red and blue curves) results in lower diffusive profile than that by the upwind method (green curve). It is also shown that the rotation by Eq. (33) with the third order rotation matrix (red curve) is very accurate even for a rather large time step Δt. The rotation by the difference form by Eq. (31) (blue curve), in contrast, shows the discretized error which depends on the choice of a time step Δt. The RCIP combined with the third order rotation matrix preserves the high transport accuracy of the tensor components.

We incorporate the semi-Lagrangian procedure not only in the flow advection, but also in the Jaumann co-rotational effect by making use of the matrix form of Eq. (32). This technique, "Co-rotated semi-Lagrangian" method, can be used with any kind of semi-Lagrangian scheme. In this paper, we will employ the CIP-CSLR, and, hereafter we will call our method as "CIP-CSLR-CS".

3.3. Integration form of viscoelastic stress by Maxwell constitutive equation

After the stress tensor $\boldsymbol{\tau}$ is advected and co-rotated by the CIP-CSLR-CS, the constitutive equation (3) reads

$$\frac{\partial \tau_{ij}}{\partial t} = -\frac{1}{\lambda}\tau_{ij} + \frac{2\eta}{\lambda} d_{ij}. \tag{34}$$

The problem now is to integrate Eq. (34) with the time step as large as possible. Here we adopt an exponential time differencing (ETD) method (e.g. [33]), in which the stretching tensor d_{ij} is approximated as constant over a time increment Δt, namely

$$\int_{\Delta t} d_{ij} \mathrm{d}t = \Delta t d_{ij}. \tag{35}$$

The assumption (35) enables us to perform the analytical integration of (34) [14];

$$\tau_{ij}^{n+1} = \tau_{ij}^{**} \mathrm{e}^{\frac{-\Delta t}{\lambda}} + 2\eta\left(1 - \mathrm{e}^{\frac{-\Delta t}{\lambda}}\right) d_{ij}^{n+1}, \tag{36}$$

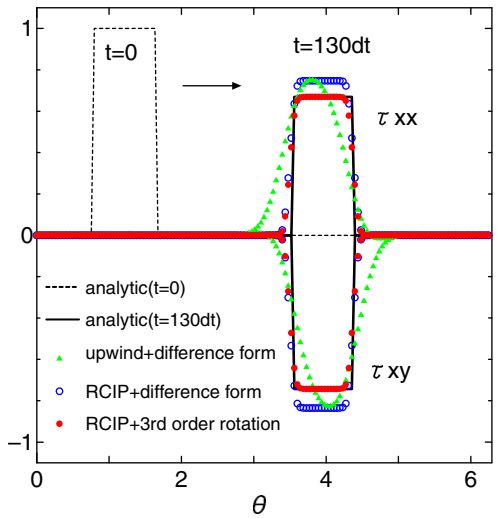

Fig. 7. Results of one-dimensional circular Jaumann co-rotational advection of square profiles of two-dimensional tensor components (τ_{xx} and τ_{xy}) under uniform angular velocity field Ω of CFL number $\Omega\Delta t/\Delta\theta$=0.5 with $\Delta\theta = 2\pi/150$. Initial distribution of τ_{xx} is given by profile named "analytic ($t = 0$)", while that of τ_{xy} is zero. Distributions of τ_{xx} and τ_{xy} after advection of 130 times steps are shown.

where τ_{ij}^{**} is the stress tensor after the co-rotational advection phase. The first term of the right-hand side of (36) is the relaxation term of a stored stress with the Maxwell relaxation time λ, and the second term is associated with the time-dependent softening of a material and the build-up of a stress by stretching. We note that this method allows us to take large Δt compared with λ as far as d_{ij} is constant during Δt.

In order to confirm the validity of (36) for large Δt, we perform calculations of a shear thinning test as illustrated in Fig. 8. The Maxwell constitutive model in a two-dimensional plane is adopted [34]. We employ a constant shearing rate of $d_{xy} = 0.05$ with a time step $\Delta t = 1.5$, which is larger than the Maxwell relaxation time $\lambda = 1$. A time evolution of deviatoric stress tensor τ_{xy} is obtained by solving (5) and (34). We consider the co-rotation of (30) by the procedure of (32) with a tenth order matrix $\boldsymbol{R}_{10}$. We neglect the advection term of Eq. (29).

Fig. 9 shows the temporal evolution of effective viscosity $\nu_{\text{eff}} = \frac{\tau_{xy}}{2d_{xy}}$, whose asymptotic limit ($t \to \infty$) is analytically given by

$$\nu_{\text{eff}}(t \to \infty) = \frac{\eta}{1 + (2\lambda d_{xy})^2} = 0.990, \tag{37}$$

owing to the Jaumann co-rotational effect. We numerically integrate Eq. (34) by three different methods; the ETD method of (36), an implicit method

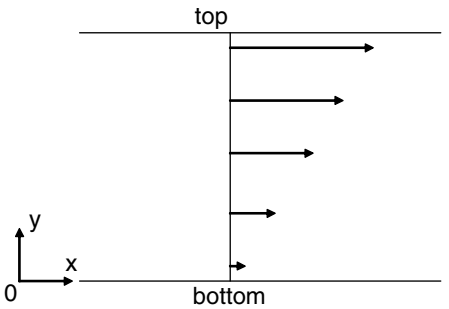

Fig. 8. Schematic picture of shear thinning test of Fig. 6. Velocity (v_x, v_y) is given by $(0.1 \times y, 0)$, and therefore $d_{xy} = 0.05$.

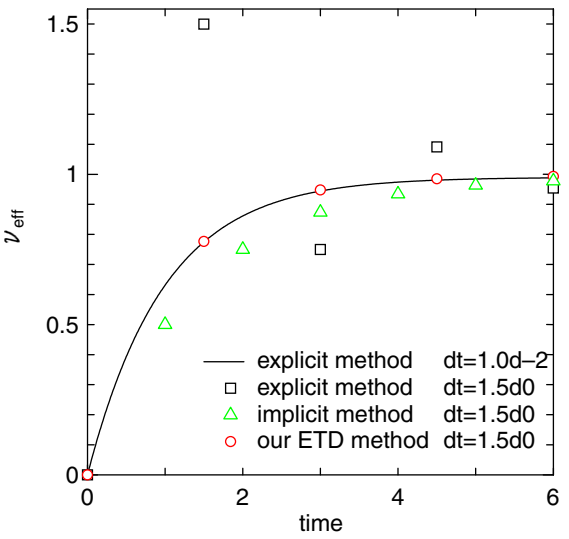

Fig. 9. Temporal evolutions of effective viscosity ν_{eff} during shear thinning test of co-rotational Maxwell viscoelastic fluid with $\eta = 1.0$, $\lambda = 1.0$ and $d_{xy} = 0.05$. Plotted are results obtained by different schemes and time step Δt.

$$\tau_{ij}^{n+1} = \tau_{ij}^{**}\frac{\lambda}{\lambda+\Delta t} + 2\frac{\eta\Delta t}{\lambda+\Delta t}d_{ij}^{n+1}, \tag{38}$$

and an explicit method

$$\tau_{ij}^{n+1} = \tau_{ij}^{**}\left(1-\frac{\Delta t}{\lambda}\right) + 2\eta\frac{\Delta t}{\lambda}d_{ij}^{n+1}. \tag{39}$$

For the comparison, the result of the explicit method with small $\Delta t = 0.01 \ll \lambda$ is also given as the reference solution (solid curve). From Fig. 9, we can see that the three methods of the time integration of (34) result in different temporal evolutions of v_{eff} with a large $\Delta t = 1.5$, although all of the methods tend to attain the same correct asymptotic state ($t \to \infty$). The explicit method (square) of Eq. (39) with the large time step shows an incorrect oscillatory behavior. The integration by the implicit method (triangle) by Eq. (38), on the other hand, does not oscillate even for the large Δt but underestimates v_{eff}. In contrast, the ETD method (circle) by (36) accurately follow the reference solution even when the large Δt is used. From this comparison we conclude that the ETD method successfully reproduces the correct viscoelastic behavior both for transient and asymptotic states, as long as the assumption (35) holds.

3.4. Solution of Stokes equation

By inserting Eq. (36) into (1), we obtain the equation for the force balance at new time step $(n+1)$ as

$$-\frac{\partial p}{\partial x_i} + \frac{\partial}{\partial x_j}(2\eta_{\text{eff}}d_{ij}) + f_{\text{eff},i} = 0, \tag{40}$$

where the effective viscosity η_{eff} and effective body force $f_{\text{eff},i}$ in ith direction are given by

$$\eta_{\text{eff}} = \eta\left(1-\mathrm{e}^{\frac{-\Delta t}{\lambda}}\right), \quad f_{\text{eff},i} = \frac{\partial}{\partial x_j}\left(\tau_{ij}^{**}\mathrm{e}^{\frac{-\Delta t}{\lambda}}\right) + f_i, \tag{41}$$

respectively. The form of Eq. (40) indicates that the viscoelastic fluid is described by a viscous fluid model with slight modifications of the viscosity and external force over a time increment Δt.

We solve the force balance Eq. (40) for the velocity $\boldsymbol{v}$ and pressure p at a new time, together with the continuity equation (2). The elliptic differential equation for $\boldsymbol{v}$ and p are solved by a multigrid method using a smoothing algorithm named "ACuTE" [35]. The ACuTE method is an extension of pseudo-compressibility method originally designed for a steady-state flow of incompressible and viscous fluid, and is proved to be suitable for convection problems with strong spatial variation of viscosity as is required in the mantle convection simulations. The details of the algorithm can be found in [36].

4. Rayleigh–Taylor instability test

4.1. Description of numerical test

We perform a three-dimensional Rayleigh–Taylor instability test, in order to demonstrate the applicability of our schemes to actual large deformation problems of a viscoelastic fluid. The initial setup is shown in Fig. 10(a) A viscoelastic fluid with the viscosity η_{upper}, with Maxwell relaxation time λ_{upper} and with density m_{upper} is initially confined in the upper half of a three-dimensional rectangular box. The lower half of the box is filled with a purely viscous fluid (called "air") with small viscosity η_{lower} and density m_{lower}. The size of the box is $0.5 \times 0.5 \times 1$, and the z-axis is in the vertical direction pointing upward. The body force of (1) by the gravity is written by $f_i = -\delta_{ij}mg$, where δ_{ij} is the Kronecker's δ symbol. A free-slip boundary condition is applied along the side walls.

Non-dimensionalization of equation is done with $x_i^* = x_i/H$, $t^* = t/(\eta_{\text{upper}}/(\Delta mgH))$, $m^* = (m - m_{\text{lower}})/\Delta m$, $\eta^* = \eta/\eta_{\text{upper}}$, $p^* = p/(\Delta mgH)$ and $\tau_{ij}^* = \tau_{ij}/(\Delta mgH)$. Here H is the height of the box and $\Delta m = m_{\text{upper}} - m_{\text{lower}}$. The force balance (1) and Maxwell constitutive equation (3) in non-dimensional form are rewritten, on dropping the asterisk, by

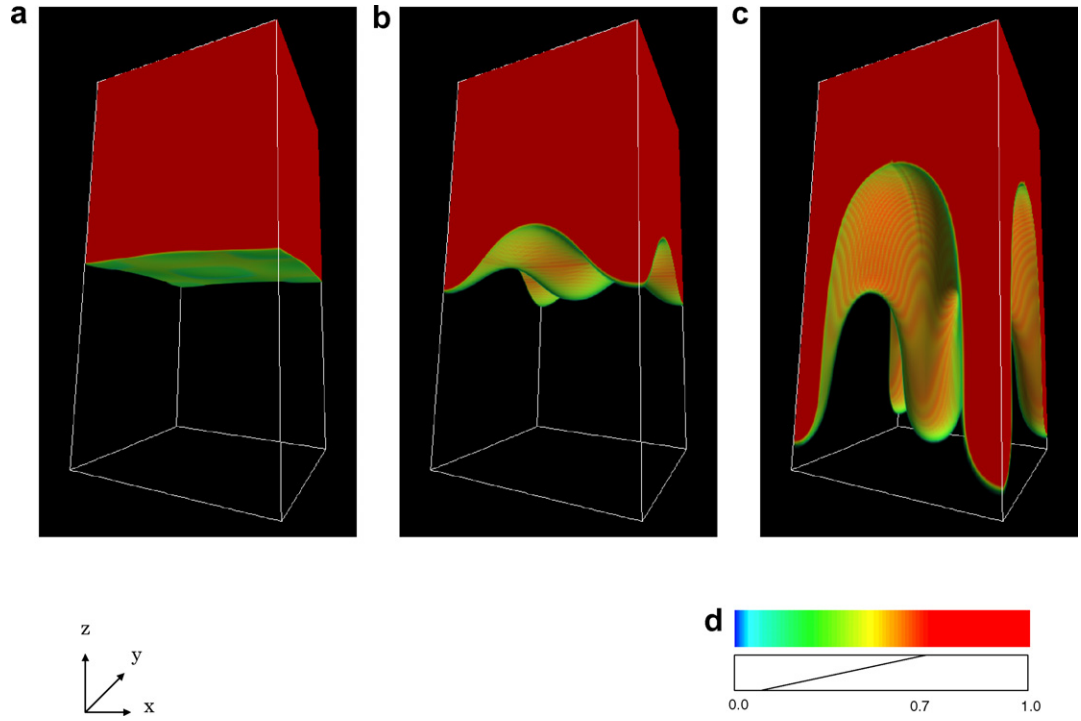

Fig. 10. Snapshots of Rayleigh–Taylor instability test in three-dimensional rectangular box with aspect ratio $0.5(x) \times 0.5(y) \times 1.0(z)$ and grid resolution of $64 \times 64 \times 128$. Shown by this volume rendering visualization is distribution of viscosity at time (a) $t = 0$, (b) $t = 100$ and (c) $t = 150$. Map of color and transparency are given in (d).

$$-\frac{\partial p}{\partial x_i} + \frac{\partial \tau_{ij}}{\partial x_j} - m\delta_{i,3} = 0, \quad \tau_{ij} + De\,\mathring{\tau}_{ij} = 2\eta d_{ij}, \tag{42}$$

where $De = \Delta mgH\lambda/\eta_{\text{upper}}$ is the dimensionless Deborah number, which is the ratio of the time scales of the stress relaxation to that of the evolution of entire system [20]. The viscosity contrast between the upper and lower layer is given by $\eta_{\text{lower}}/\eta_{\text{upper}} = 10^{-3}$. Here a color function $\Phi(\boldsymbol{x})$ is introduced to distinguish the viscoelastic fluid and air in Eq. (42), and is initially given by

$$\Phi^0(\boldsymbol{x}) = \begin{cases} 1 & \text{in upper viscoelastic fluid,} \\ 0 & \text{in air.} \end{cases} \tag{43}$$

A transport of the color function by the CIP-CSLR method represents a motion of the viscoelastic fluid and air. The non-dimensional density m^n, viscosity η^n and Deborah number De^n at nth time step in Eq. (42) are simply defined by

$$m^n(\boldsymbol{x}) = \Phi^n(\boldsymbol{x}), \eta^n(\boldsymbol{x}) = (1 - \Phi^n(\boldsymbol{x}))\eta_{\text{lower}}/\eta_{\text{upper}} + \Phi^n(\boldsymbol{x}), \tag{44}$$

$$De^n(\boldsymbol{r}) = De_0\Phi^n(\boldsymbol{x}), \tag{45}$$

where $De_0 = \Delta mgH\lambda_{\text{upper}}/\eta_{\text{upper}}$. Similarly, the deviatoric stress tensor τ_{ij} is also transposed by the CIP-CSLR-CS method. The stress free condition $\tau_{ij}^0 = 0$ is initially employed, and the components (i.e. $\rho, S_{xy}, \sigma_x, \ldots, f$) of τ_{ij} are updated in the non-advection term by (36). By using the ACuTE method in Section 3.4, we solve the force balance of (42) between the viscoelastic fluid and air, represented by the CIP-CSLR profile.

A profile of the interface between the two fluids is initially perturbed with an amplitude of 0.005 and horizontal wave numbers $(k_x = 4\pi, k_y = 4\pi)$, which is obtained by the advection calculation for 20 time steps with $\Delta t = 1.0$ by the velocity $(v_x, v_y, v_z) = (0, 0, -2.5 \times 10^{-4}\cos(4\pi x)\cos(4\pi y))$, where the origin $(x, y, z) = (0, 0, 0)$ is defined at the center of the box. It must be emphasized that the amplitude of perturbation (0.005) of the

initial profile is comparable to the grid size resolution ($\Delta z = 1/128 \simeq 0.007$ for the typical grid size $64 \times 64 \times 128$ of this paper), which implies that a quantitative treatment of this instability needs numerical schemes which can handle the profile of the fluid interface with a spatial resolution smaller than the grid size.

We present in Fig. 10(b) and (c) the snapshots of the distribution of the viscoelastic fluid at $t = 100$ and at $t = 150$, respectively. The figures show that the calculation by our semi-Lagrangian scheme successfully captures the sharp boundary of the material qualitatively. In what follows, we validate our methods by quantitative comparisons with the semi-analytical solution of this instability [13]. In order to make a numerical estimate of an instability amplitude, we employed a particle tracer which was initially placed at the center of the fluid interface. The instability amplitude is determined by the displacement of the particle from its initial position.

4.2. Impact of CIP-CSLR in Viscous deformation

We will first focus on the results of the case with a purely viscous fluid ($De = 0$), where our semi-Lagrangian scheme only transports a scalar variable (i.e. $\Phi(\boldsymbol{x})$). The instability amplitude grows as $e^{\omega t}$ in the linear stability analysis of a viscous deformation.

In order to see the applicability of our scheme combined with the CIP-CSLR to the present calculation, Table 3 provides the comparison of growth rates ω by various resolutions and advection procedures in the calculation. The results of our CIP-CSLR treatment, with the raw velocity of (20) and flux corrections of (28), are in good agreement with theoretical one, even in the lowest resolution case of $32 \times 32 \times 64$.

For the purpose of showing the effect of a conservation of fluid mass on this problem, we also present the result with (non-conservative) RCIP advection scheme. Although both of semi-Lagrangian schemes (RCIP and CIP-CSLR) can capture a sharp surface of the profile like Fig. 10, a quantitative comparison of ω shows that the result with the RCIP scheme deviates from the theoretical estimate. Since the growth of the Rayleigh–Taylor instability during the very initial stage is strongly sensitive to the mass distribution of a sub-grid scale, a loss or gain of a fluid mass in RCIP spoils the accuracy of the results. In contrast, the mass conservation of CIP-CSLR method largely contributes to the good accuracy of our method.

We also show the results by changing the process of CIP-CSLR in Table 3, so as to elucidate how our CIP-CSLR advection by the raw velocity with the flux correction works.

When we compare the results of two velocity settings for the staggered grid system (i.e. raw velocity and averaged velocity), the growth rate by the raw velocity shows better agreement with the analytic one. This is because the averaged velocity method have the diffusiveness discussed in Section 3.1.4.

On the other hand, if we turn off the flux corrections of (27) and (28), a negligible value of the negative profile is obtained in the beginning of this calculation (e.g., $\Phi_{\min} \sim -10^{-32}$ at $t = 5$), and the growth rate by the raw velocity is almost the same with that of our method. This indicates that our flux correction scheme does not change the solution, if the normal CIP-CSLR works well without unwanted negative profile. In other words, when we solve the problems under the proper deformation and physical model, which do not cause a deep valley in a sub-grid profile, our flux correction method is not necessary.

However, after the long time calculation over the time range of above linear stability analysis, a separation of deep valley with negative value is induced by the force balance without the flux correction as is shown in

Table 3
Comparison of growth rates ω of Rayleigh–Taylor instability test with $De = 0$

Calculation method	Mesh size	ω
Semi-analytic		2.81×10^{-2}
RCIP	$32 \times 32 \times 64$	1.60×10^{-2}
CIP-CSLR		
By raw velocity with flux corrections	$128 \times 128 \times 256$	2.771×10^{-2}
By raw velocity with flux corrections	$64 \times 64 \times 128$	2.767×10^{-2}
By raw velocity with flux corrections	$32 \times 32 \times 64$	2.74×10^{-2}
By raw velocity without flux corrections	$32 \times 32 \times 64$	2.74×10^{-2}
By averaged velocity without flux corrections	$32 \times 32 \times 64$	2.67×10^{-2}

Value of ω are calculated by fitting evolution of instability amplitude from time $t = 1$–5.

Fig. 11: there are the negative value spots represented by the white isosurface. Our flux correction corrects the profiles of these negative regions.

In our target plate-mantle simulation, such a deviation of deep valley may occur in the temporal advection step in the complex flows, or in a physical modeling of material (e.g., production of plate, brittle breaking and phase changes), which will be employed as non-advection terms. Our flux correction method is reasonable method of dealing with these problems, because it guarantees the positiveness of a profile, whatever the reason for making valley profile is, without losing the low diffusiveness of CIP-CSLR.

4.3. Growth by viscoelastic deformation

Now we compare temporal evolutions of instability amplitude calculated for two cases with Deborah numbers $De = 0.05$ and 2.5 in Fig. 12. For the case with $De = 2.5$, the temporal evolution of instability exhibits two stages. In the first stage (elastic mode), the amplitude increases very rapidly owing to the effect of an elastic softening. (The behavior of this elastic mode will be discussed in detail in the next subsection.) In the second stage of the deformation (viscous mode), where the viscous deformation is dominant, the instability grows at an almost constant rate. The deformation mechanism changes with time from the elastic mode to the viscous ones due to the time evolution of a viscoelastic stress by Eq. (36). On the other hand, in the case of $De = 0.05$ where the elastic effect is negligible, the first stage of the elastic mode almost vanishes. The temporal evolution of instability is thus quite similar to that obtained for the case with purely viscous deformation.

We calculated the growth rate ω of the instability during the viscous mode. In Table 4, we compare the values of ω obtained by our simulation with those from the theoretical estimates by [13]. Our results are in good agreement with the theoretical estimates and successfully reproduce the dependence of ω on De. The instability of viscous mode grows faster for a larger De.

4.4. Instantaneous growth by elastic deformation

Here we analyze the first stage of the elastic deformation. Fig. 13 shows the behavior of the elastic deformation mode in detail: The temporal evolution of instability for $De = 2.5$ in the very early stage. At the beginning of the deformation, the effective viscosity of Eq. (41) becomes very small owing to the elasticity, and the

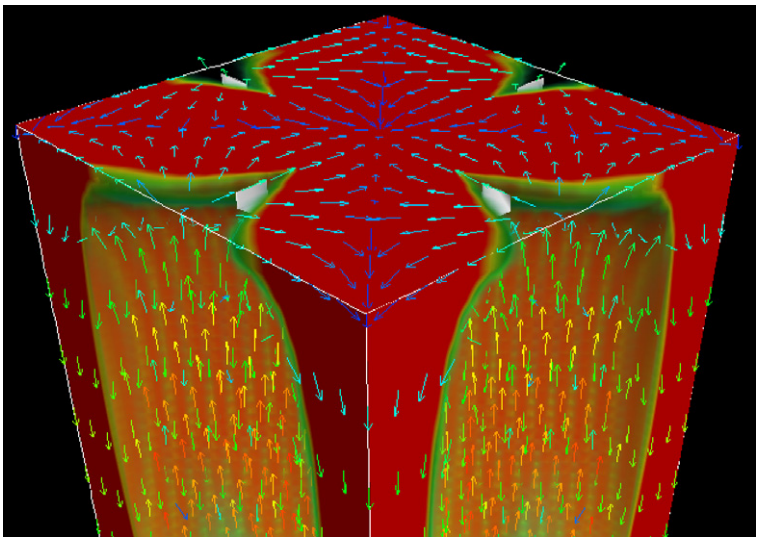

Fig. 11. Top view of Rayleigh–Taylor instability calculation at $t = 230$ with grid resolution of $32 \times 32 \times 64$. CIP-CSLR with raw velocity without flux corrections is employed as advection method. Distribution of viscosity is shown in the same way as Fig. 10 with velocity arrows. In addition, negative value profile at $\Phi = -0.001$ is represented by white isosurface. Minimum value of this profile is $\Phi_{\min} = -0.018$.

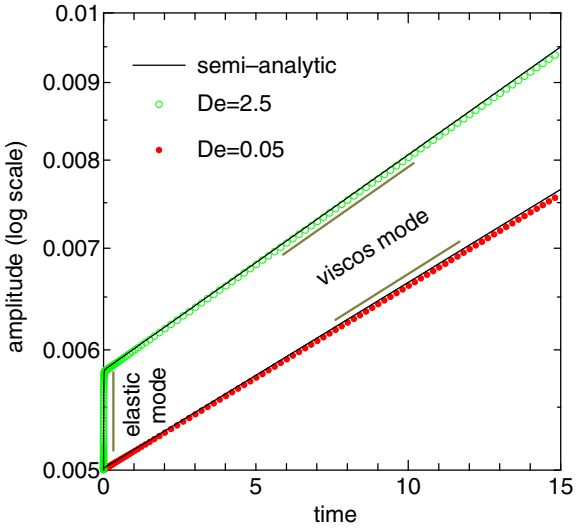

Fig. 12. Temporal evolutions of instability amplitude of three-dimensional Rayleigh–Taylor instability for viscous fluid for viscoelastic fluid with Deborah number $De = 0.05$ and $De = 2.5$. Grid resolutions is $64 \times 64 \times 128$.

Table 4
Comparison of growth rates ω obtained by present numerical tests and those from semi-analytic study

	$De = 0.05$	$De = 2.5$
ω of our result	2.78×10^{-2}	3.26×10^{-2}
ω of semi-analytic result	2.82×10^{-2}	3.27×10^{-2}

Value of ω are calculated by fitting evolution of instability amplitude from time $t = 1$–5, shown in Fig. 12.

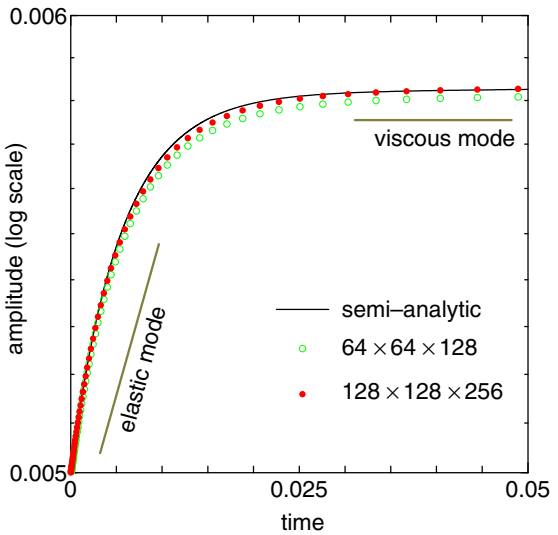

Fig. 13. Same as Fig. 12 but for viscoelastic fluid with Deborah number $De = 2.5$ during very early stage ($t \leqslant 0.05$) calculated by grid resolutions of $64 \times 64 \times 128$ and $128 \times 128 \times 256$.

viscoelastic fluid in the upper layer is extremely softened and free from an internal resistance by the viscoelastic stress. In the elastic mode, therefore, a viscous resistance of the soft fluid in the lower layer must be balanced with a gravity force acting on the upper layer through the interface. In other words, the interface deforms rap-

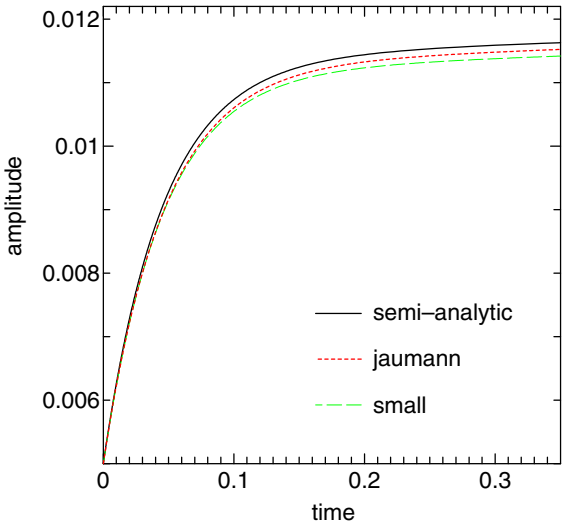

Fig. 14. Same as Fig. 12 but for viscoelastic fluid with Deborah number $De = 10.0$ calculated with (labeled "jaumann") or without ("small") Jaumann co-rotational effect. Grid resolutions is $64 \times 64 \times 128$. Vertical axis is in linear scale in this plot.

idly so that the viscous resistance of the lower layer with the small viscosity satisfies the force balance. This is the reason why the instability amplitude develops very fast in the elastic mode. This elastic mode continues until the viscoelastic stress (36) is accumulated enough to make the internal resistance of the upper layer be balanced with the gravity force, indicating that the transition of deformation mode to the viscous mode takes place.

The instability amplitude calculated by our methods with a finer grid resolution of $128 \times 128 \times 256$ (red circle) is in good agreement with the theoretical estimate. On the other hand, the solution with the grid size of $64 \times 64 \times 128$ (green opened circle) shows a slight disagreement with the theoretical value. We have found that this error is related to a numerical oscillation of the deviatoric stress tensor caused by the rapid deformation of the viscoelastic fluid. A further improvement would be required in order to resolve an instantaneous elastic response with better accuracy.

4.5. Effects of Jaumann co-rotational term

In order to quantify the importance of the Jaumann co-rotational effect, we also perform calculations where the co-rotational term (30) is turned off. It is found that the results are quite similar to those with the co-rotational term for both $De = 0.05$ and 2.5 cases. It is because the effect of an elasticity is too small in the present numerical experiment. Indeed, as shown in Fig. 14, the co-rotational effect is very minor in resisting the deformation even for the case with $De = 10.0$ where the effect of the elasticity is significantly emphasized.

5. Summary

We have developed a simulation scheme for a finite deformation of viscoelastic fluids in the Eulerian frame of reference. In order to capture sharp surfaces in the material, we apply the CIP-CSLR method as a semi-Lagrangian scheme. The fractional step technique is employed to advect three-dimensional scalar and tensor profiles on the staggered grid. In addition, the flux correction method is proposed for advecting a slowly moving non-negative profile. Our scheme automatically detects the appearance of a numerical oscillation near the zero level, and applies the diffusive or clipping corrections to the numerical error. As for the Maxwell constitutive equation, we propose "Co-rotated semi-Lagrangian" method, in which the Jaumann co-rotational term are solved by the semi-Lagrangian method with rotation of the tensor components by the rotation matrix. The residual time integration of the Maxwell viscoelasticity is done by the ETD method. The combination of these

techniques enables us to integrate the Maxwell constitutive equation with large time step Δt, keeping high numerical accuracy as long as the velocity does not change significantly over the time increment Δt.

Generally, the computer code based on Eulerian methods are easier in the optimization of the vectorization/parallelization than (semi-) Lagrangian treatments with (remapping) remeshing procedures. Since our scheme is based on the fully Eulerian procedure of the CIP-CSLR, our code can attain high performance on massively vector/parallel super computers.

We have applied our method to the three-dimensional model via the spatial dimensional splitting method of the CIP-CSLR. We have performed a three-dimensional simulation of viscoelastic Rayleigh–Taylor instability and confirmed the qualitative and quantitative validity of our scheme.

In order to fully address the question how the elasticity affects the plate tectonics, it is inevitable to incorporate non-linear deformation mechanisms other than elasticity. The results of our numerical experiments are consistent with the earlier finding of the viscoelastic studies that the elastic property with the rotational term does not play an essential role in the actual gravitational deformation processes of the plates ($De \leqslant 0.1$) [13,20], although it may cause several side-effects [15,18,34]. However, even though the elastic deformation itself is negligible, the elastically-stored stress (with the advection and rotation) may influence the non-linear deformation mechanisms of the plates, because some of them strongly depend on the stress state of a material (e.g., triggering brittle behavior). In order to clarify such roles of the viscoelastic stress in rheological properties of the plates, we need further investigation of modeling non-linear rheologies.

Acknowledgments

We thank Boris J.P. Kaus and Xindong Peng for fruitful discussion. All of the numerical calculations presented in this paper were performed by Earth Simulator of Japan Agency for Marine-Earth Science and Technology.

Appendix A. Diffuse-flow correction in CIP-CSLR method

In order to understand the details of the diffuse-flow correction in Section 3.1.5, we discuss what kind of rational function profile (13) is corrected by (28). In the following we restrict ourselves to the advection of a profile around $x = x_i$ under a uniform flow $v > 0$ and assume $f_{iup=i-1} \leqslant S_{i-\frac{1}{2}} = \rho_{i-\frac{1}{2}}/|\Delta x| \leqslant f_i$, where the spatial integral D_i^n can be calculated by (28) with the values of the downstream f_i and upstream f_{i-1} sides and the cell integrated value $\rho_{i-\frac{1}{2}}$. We define a dimensionless parameter α as

$$\alpha = \frac{|D_i^n(x_i - \mathrm{CFL}\Delta x)|}{\rho_{i-\frac{1}{2}}^n} = \frac{(\phi_1^2\phi_2 - 1)(\mathrm{CFL})^2 + \phi_1(1 - \phi_1\phi_2)(\mathrm{CFL})}{1 - \phi_1\phi_2 + \mathrm{CFL}(\phi_1 + \phi_1\phi_2 - 2)}, \tag{A.1}$$

where $\mathrm{CFL} = v\Delta t/\Delta x$, $\phi_1 = f_i^n/S_{i-\frac{1}{2}}$, and $\phi_2 = f_{i-1}^n/f_i^n$. The diffuse-flow correction Eq. (28), becomes active when $\alpha \geqslant \alpha_c$.

In Fig. A.1, we plot a contour map of the nondimensional parameter α on the ϕ_1–ϕ_2 plane. Fig. A.1(a) shows the case for $\mathrm{CFL} = 0.2$. When $\alpha_c = 0.5$ (black curve) that the inequality $\phi_1 \geqslant 3.4$ is the necessary condition for $\alpha \geqslant \alpha_c$. Since $S_{i-\frac{1}{2}}$ is the averaged value, $\phi_1 = f_i/S_{i-\frac{1}{2}} \geqslant 3.4$ means that the value at downstream side f_i is relatively large compared with the mean profile. It is also clear in Fig. A.1(a) that the condition $\alpha \geqslant \alpha_c$ leads to small value of $\phi_2 = f_{i-1}/f_i < 0.08$: The value of the upstream side f_{i-1} must be sufficiently smaller than that of the downstream side f_i. These constraints indicate that the diffuse-flow correction of (28) becomes active only when the profile have a very steep gradient in the cell.

Fig. A.1(b) shows that the contour of CFL number for fixed $\alpha = \alpha_c = 0.5$. It is obvious that our criterion of $\alpha \geqslant \alpha_c$ strongly depends on the CFL number of the calculation. With increasing the CFL number, the flux corrected region ($\alpha \geqslant \alpha_c$) on the ϕ_1–ϕ_2 plane becomes large, and at last for the case of $\mathrm{CFL} = 0.5$ (light blue curve) any profile of $\phi_2 \leqslant 1/\phi_1$ (i.e., $f_{i-1} \leqslant S$) is corrected by (28). This indicates that the diffuse-flow correction of Eq. (28) with a large CFL number works not only on an oscillation part, but also on a non-oscillation part of the profile in a diffusive manner. For the purpose of preserving a good sharpness of the CIP-CSLR profile, we should employ a small CFL number in our correction scheme (< 0.2, for example).

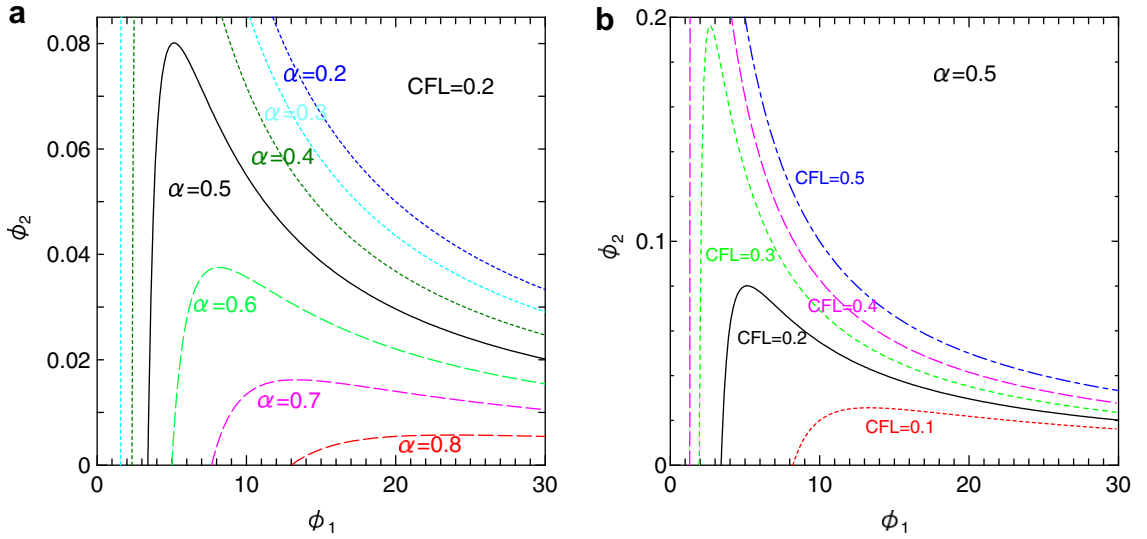

Fig. A.1. Plots as function of ϕ_1 and ϕ_2 of (a) nondimensional parameter a for fixed CFL number of 0.2, and (b) CFL for fixed $\alpha = \alpha_c = 0.5$. See text for definitions of variables.

An additional care must be taken when applying the above technique to multi-dimensional calculations. For two- or three-dimensional calculations, a smaller α_c should be preferred (e.g., $\alpha_c = 1/6$ for three-dimensional cases) due to the increase of the cell faces. As shown in Fig. A.1(a), however, it is difficult to preserve the shape with small α_c because it causes strong diffusive effects. The calculations with a smaller α_c need a smaller CFL number to maintain the shape preservation of a profile (see also Fig. A.1(b)). Instead, we perform the multi-dimensional calculation by a directional splitting method in Section 3.1.3, in which the one-dimensional advection with $\alpha_c = 0.5$ can be applied to every direction. This technique successfully reproduces a low diffusive shape of solution even for multi-dimensional simulations with the same CFL number as one-dimensional case.

Appendix B. Implement of Jaumann co-rotational derivative

In order to incorporate the Jaumann co-rotational term into a semi-Lagrangian method, we derive the expression of the Jaumann rate, i.e., the rate of tensor from a view of observer who rotates with the material point.

The difference in the views from different observers can be represented by the change of the base vector $\boldsymbol{g}$ from time t to γ as

$$\boldsymbol{g}^i[\gamma] = \boldsymbol{R}_t[\gamma]\boldsymbol{g}^i[t], \tag{B.1}$$

where $\boldsymbol{R}_t[\gamma] = \boldsymbol{g}^i[\gamma] \otimes \boldsymbol{g}^i[t]$ is the rotation tensor. With this notation, a tensor $\boldsymbol{\tau}$ at time γ is defined as

$$\boldsymbol{\tau} = \tilde{\tau}_{ij}\boldsymbol{g}^i[\gamma] \otimes \boldsymbol{g}^j[\gamma] \tag{B.2}$$

$$= \boldsymbol{R}_t[\gamma]\tilde{\tau}_{ij}\boldsymbol{R}_t^{\mathrm{T}}[\gamma]\boldsymbol{g}^i[t] \otimes \boldsymbol{g}^j[t] \tag{B.3}$$

$$= \tau_{ij}\boldsymbol{g}^i[t] \otimes \boldsymbol{g}^j[t]. \tag{B.4}$$

The Jaumann co-rotational rate of $\boldsymbol{\tau}$ is the material derivative of $\tilde{\tau}_{ij}$, defined with the fixed base vector $\boldsymbol{g}^i[t]$. The material derivative of Eqs. B.2, B.3 and B.4 with time γ is

$$\dot{\boldsymbol{\tau}} = (\tilde{\tau}_{ij}\boldsymbol{g}^i[\gamma] \otimes \boldsymbol{g}^j[\gamma])^{\cdot} \tag{B.5}$$

$$= (\boldsymbol{R}_t[\gamma]\tilde{\tau}_{ij}\boldsymbol{R}_t^{\mathrm{T}}[\gamma])^{\cdot}\boldsymbol{g}^i[t] \otimes \boldsymbol{g}^j[t] \tag{B.6}$$

$$= \dot{\tau}_{ij}\boldsymbol{g}^i[t] \otimes \boldsymbol{g}^j[t], \tag{B.7}$$

here dot denotes the material derivative. By taking the limit of $\gamma \to t$ in Eq. (B.6), the usual Jaumann co-rotational form is derived

$$\boldsymbol{\tau} \overset{\circ}{=} \dot{\tilde{\tau}}_{ij}\boldsymbol{g}^i[t] \otimes \boldsymbol{g}^j[t] = (\dot{\tau}_{ij} - w_{ik}\tau_{kj} + \tau_{ik}w_{kj})\boldsymbol{g}^i[t] \otimes \boldsymbol{g}^j[t] = \dot{\boldsymbol{\tau}} - \boldsymbol{w}\cdot\boldsymbol{\tau} + \boldsymbol{\tau}\cdot\boldsymbol{w}, \tag{B.8}$$

where $\boldsymbol{w} = \lim_{\gamma\to t}\dot{\boldsymbol{R}}_t[\gamma]$ is spin tensor.

On the other hand, Jaumann co-rotational derivative can be written as an advection equation from (B.3) and (B.4), as follows

$$\boldsymbol{\tau} \overset{\circ}{=} (\boldsymbol{R}_t^{\mathrm{T}}[\gamma]\tau_{ij}\boldsymbol{R}_t[\gamma])^{\cdot}\boldsymbol{g}^i[t] \otimes \boldsymbol{g}^j[t]. \tag{B.9}$$

Eq. (B.9) is the advection form of the tensor $\boldsymbol{F} = \boldsymbol{R}_t^{\mathrm{T}}[\gamma]\cdot\tau_{ij}\cdot\boldsymbol{R}_t[\gamma]$, and can be solved in the advective procedure of a semi-Lagrangian scheme as follows

$$\boldsymbol{F}^t(\boldsymbol{x}) = \boldsymbol{F}^{t-\Delta t}(\boldsymbol{x} - \boldsymbol{v}\Delta t) \tag{B.10}$$

$$= \boldsymbol{R}_{t-\Delta t}^{\mathrm{T}}[t]\cdot\tau_{ij}[t-\Delta t](\boldsymbol{x} - \boldsymbol{v}\Delta t)\cdot\boldsymbol{R}_{t-\Delta t}[t], \tag{B.11}$$

where the rotation tensor $\boldsymbol{R}_{t-\Delta t}[t]$ is obtained by

$$\boldsymbol{R}_{t-\Delta t}[t] = \mathrm{e}^{\boldsymbol{w}\Delta t}, \tag{B.12}$$

under the assumption that $\frac{\partial \boldsymbol{v}}{\partial t} = 0$.

References

[1] F.D. Stacey, Physics of the Earth, Brookfield Press, Australia, 1992, p. 513.
[2] D.L. Turcotte, G. Schubert, Geodynamics, second edition., Cambridge University Press, 2002, 456 p.
[3] S. Uyeda, Subduction zones: an introduction to comparative subductology, Tectonophysics 81 (1982) 133–159.
[4] W.M. Kaula, R.J. Phillips, Quantitative tests for plate tectonics on Venus, Geophys. Res. Lett. 8 (1981) 1187–1190.
[5] D.L. Turcotte, E.R. Oxburgh, Finite amplitude convection cells and continental drift, J. Fluid Mech. 28 (1967) 29–42.
[6] D.P. McKenzie, J. Roberts, N.O. Weiss, Convection in the Earth's mantle, Tectonophysics 19 (1973) 89–103.
[7] P.J. Tackley, Mantle convection and plate tectonics: toward an integrated physical and chemical theory, Science 288 (5473) (2000) 2002–2007.
[8] D. Bercovici, The generation of plate tectonics from mantle convection, Earth Planet. Sci. Lett. 205 (3–4) (2003) 107–121.
[9] G. Schubert, D.L. Turcotte, P. Olson, Mantle Convection in the Earth and Planets, Cambridge University Press, 2001, 940 p.
[10] S.K. Godunov, Finite-difference method for the numerical computation of discontinuous solutions of the equations of gas dynamics, Mat. Sb. 47 (1959) 271–306.
[11] P. Wesseling, Principles of Computational Fluid Dynamics, Springer Series in Computational Mathematics, vol. 29, 2001, 339 p.
[12] H. Harder, Numerical simulation of thermal convection with Maxwellian viscoelasticity, J. Non-Newton. Fluid Mech. 39 (1991) 67–88.
[13] B.J.P. Kaus, T.W. Becker, Effects of elasticity on the Rayleigh–Taylor instability: implications for large-scale geodynamics, Geophys. J. Int. 168 (2007) 843–862.
[14] R.C. Bailey, Large time step numerical modelling of the flow of Maxwell materials, Geophys. J. Int. 164 (2006) 460–466.
[15] F. Funiciello, G. Morra, K. Regenauer-Lieb, D. Giardini, Dynamics of retreating slabs: 1. Insights from two-dimensional numerical experiments, J. Geophys. Res. 108 (2003) 2206.
[16] P.J. Tackley, S. Xie, Stag3D: a code for modeling thermo-chemical multiphase convection in Earth's mantle, in: K.J. Bathe (Ed.), Proceedings of the Second MIT Conference on Computational Fluid and Solid Mechanics, Elsevier B.V., Amsterdam, 2003, pp. 1524–1527.
[17] L. Moresi, F. Dufour, H.B. Muhlhaus, A Lagrangian integration point finite element method for large deformation modeling of viscoelastic geomaterials, J. Comput. Phys. 184 (2003) 476–497.
[18] L. Moresi, F. Dufour, H.B. Muhlhaus, Mantle convection modeling with viscoelastic/brittle lithosphere: numerical methodology and plate tectonic modeling, Pure Appl. Geophys. 159 (2002) 2335–2356.
[19] S.M. Schmalholz, Y.Y. Podladchikov, D.W. Schmid, A spectral/finite difference method for simulating large deformations of heterogeneous, viscoelastic materials, Geophys. J. Int. 145 (2001) 199–208.
[20] A.N.B. Poliakov, P.A. Cundall, Y.Y. Podladchikov, V.A. Lyakhovsky, An explicit internal method for the simulation of viscoelastic flow: an evaluation of elastic effects on diapiric flow in two- and three- layers models, in: D.B. Stone, S.K. Runcorn (Eds.), Proceedings of NATO Advanced Study. Institute, Flow and Creep in the Solar System: Observations, Modeling and Theory, 1993, pp. 175–195.
[21] H. Takewaki, A. Nishiguchi, T. Yabe, Cubic interpolated pseudo-particle method (CIP) for solving hyperbolic-type equations, J. Comput. Phys. 61 (1985) 261–268.
[22] T. Yabe, T. Ishikawa, P.Y. Wang, T. Aoki, Y. Kadota, F. Ikeda, A universal solver for hyperbolic equations by cubic-polynomial interpolation II. Two- and three- dimensional solvers, Comput. Phys. Commun. 66 (1991) 233–242.

[23] F. Xiao, T. Yabe, T. Ito, Constructing oscillation preventing scheme for the advection equation by a rational function, Comput. Phys. Commun. 93 (1996) 1–12.
[24] F. Xiao, T. Yabe, G. Nizam, T. Ito, Constructing a multi-dimensional oscillation preventing scheme for the advection equation by a rational function, Comput. Phys. Commun. 94 (1996) 103–118.
[25] T. Yabe, R. Tanaka, T. Nakamura, F. Xiao, An exactly conservative semi-Lagrangian scheme (CIP-CSL) in one dimension, Mon. Weather Rev. 129 (2001) 332–344.
[26] T. Nakamura, R. Tanaka, T. Yabe, K. Takizawa, Exactly conservative semi-Lagrangian scheme for multi-dimensional hyperbolic equations with directional splitting technique, J. Comput. Phys. 174 (2001) 171–207.
[27] F. Xiao, T. Yabe, Completely conservative and oscillationless semi-Lagrangian schemes for advection transportation, J. Comput. Phys. 170 (2001) 498–522.
[28] F. Xiao, T. Yabe, X. Peng, H. Kobayashi, Conservative and oscillation-less atmospheric transport schemes based on rational functions, J. Geophys. Res. 107 (D22) (2002) 4609.
[29] F. Xiao, X. Peng, A convexity preserving scheme for conservative advection transport, J. Comput. Phys. 170 (2004) 389–402.
[30] B. Bermejo, A. Staniforth, The conversion of semi-Lagrangian advection schemes to quasi-monotone schemes, Mon. Weather Rev. 120 (1992) 2622–2632.
[31] S.T. Zalesak, Fully multidimensional flux-corrected transport algorithms for fluids, J. Comput. Phys. 31 (1979) 335–362.
[32] F. Xiao, T. Yabe, Computation of complex flows containing rheological bodies, CFD J. 8 (1999) 43–49.
[33] S.M. Cox, P.C. Matthews, Exponential time differencing for stiff systems, J. Comput. Phys. 176 (2002) 430–455.
[34] H.B. Muhlhaus, K. Regenauer-Lieb, Towards a self-consistent plate mantle model that includes elasticity: simple benchmarks and application to basic modes of convection, Geophys. J. Int. 163 (2005) 788–800.
[35] M. Kameyama, A. Kageyama, T. Sato, Multigrid iterative algorithm using pseudo-compressibility for three-dimensional mantle convection with strongly variable viscosity, J. Comput. Phys. 206 (2005) 162–181.
[36] M. Kameyama, ACuTEMan: a multigrid-based mantle convection simulation code and its optimization to the Earth simulator, J. Earth Simulator 4 (2005) 2–10.